

Transversely isotropic membrane shells with application to mitral valve mechanics. Constitutive modelling and finite element implementation

V. Prot¹, B. Skallerud^{1,*},[†] and G. A. Holzapfel²

¹*Department of Structural Engineering, Norwegian University of Science and Technology, Trondheim, Norway*

²*Department of Solid Mechanics, Royal Institute of Technology, Stockholm, Sweden*

SUMMARY

The present study addresses constitutive modelling and implementation of transversely isotropic hyperelastic material models for the analysis of the mitral valve. This valve separates the left atrium and left ventricle in the heart. Two convex strain energy potentials are employed in derivation of stress tensors and elasticity tensors. The plane stress and incompressibility conditions are accounted for directly. The relationships are implemented in an implicit code (ABAQUS) *via* the user-defined interface. Numerical simulations of the valve motion during a part of the heart cycle are carried out and compared to ultrasound measurements of a healthy human valve. The significance of placement of chordae tendinae is illustrated. The implementation provides a tool for simulations of both healthy and pathological mitral valve conditions. Copyright © 2007 John Wiley & Sons, Ltd.

Received 14 July 2006; Revised 11 December 2006; Accepted 12 December 2006

KEY WORDS: hyperelasticity; transverse isotropy; membrane shells; biomechanics; mitral valve

1. INTRODUCTION

In many instances a three-dimensional finite element approach is employed for the analysis of soft biological tissues. Frequently, soft tissues are considered as incompressible (or nearly incompressible) materials, and this constraint is then treated by means of the mixed finite element method. However, several soft tissues show a significant large planar extension and a much smaller extension in the out-of-plane direction, so that the stress state can be considered as plane. Such tissue sheets can conveniently be analysed using structural elements such as membrane shell finite elements.

*Correspondence to: B. Skallerud, Department of Structural Engineering, Norwegian University of Science and Technology, Trondheim, Norway.

[†]E-mail: bjorn.skallerud@ntnu.no

In such elements the plane stress condition is accounted for leading to simulations in a reduced stress space. The incompressibility condition is used to express the strain in the out-of-plane direction as a function of the in-plane strains, and there is no need to use mixed finite elements.

The present work was motivated by an interest in the development of an accurate and robust constitutive framework for the large deformation behaviour of those soft biological tissues, which may be characterized by a single family of collagen fibres. In particular, the focus was on the implementation of two constitutive models able to capture the typical stress–strain response of mitral valves. For this purpose the non-linear finite element program ABAQUS/standard and the user-defined subroutine UMAT served as an appropriate tool. The main interest, however, was the numerical simulation of the mitral valve/chordae tendinae complex.

The mitral valve is a very important valve between the left atrium and the left ventricle of the heart. It consists of two leaflets: the anterior (or aortic, as it is located close to aorta) and the posterior. The anterior leaflet is much larger than the posterior leaflet. Both leaflets are attached to the annulus and to the chordae tendinae. The chordae tendinae are further attached to the papillary muscles. This composition of tissues is called the mitral apparatus. During the systole the mitral apparatus prevents blood from flowing back into the atrium when the ventricle contracts. Hence, it is of major importance in order to avoid regurgitation. In order to assess pathologies, one first needs to thoroughly understand the normal heart and its tissue components. Almost all soft biological tissues such as the myocardium, tendons, heart valves and arteries exhibit anisotropic, viscoelastic and highly non-linear stress–strain responses. They undergo large deformations *in vivo* and complex coupling between their different constituents. Due to this complex material behaviour and due to the different responses between the *in vivo* and *in vitro* situations the identification of the most feasible material model and related parameters are challenging tasks.

May-Newman and Yin [1] proposed a transversely isotropic material law for mitral valve tissue. It is based on experimental data obtained from biaxial tension tests carried out on porcine mitral valves. These tests demonstrated that both leaflets are anisotropic and exhibit highly non-linear mechanical response. In [1] the focus was on *in vitro* biaxial testing of mitral valve tissue, and on the important identification of a strain-energy function and material parameters, but not on its implementation.

Hyperelasticity provides an ideal framework for numerical modelling of soft biological tissues because it allows the formulation of large deformation including anisotropic effects. Previously, several numerical simulations of the mitral apparatus have been conducted with different types of material models for the leaflets (see, e.g. Kunzelman *et al.* [2], Einstein *et al.* [3], Votta *et al.* [4], Dal Pan *et al.* [5]). Several authors have implemented models for soft biological tissues into finite element codes. Einstein *et al.* [6], e.g. described the implementation of a membrane formulation for soft tissues in an explicit finite element code. Gruttmann and Taylor [7] derived a rubberlike constitutive material model for membrane shells using principal stretches, whereas the present work is based on an invariant formulation. Holzapfel *et al.* [8] described a finite element implementation of the Fung model for biological membranes. Weiss *et al.* [9] provided an implementation of nearly incompressible transversely isotropic hyperelastic materials, and Sun and Sacks [10] implemented a generalized Fung model more recently.

In the present study, we develop a generalized approach for a finite element implementation of transversely isotropic membrane shells with application to mitral valve leaflet mechanics. The formulation of transversely isotropic hyperelasticity is based on the account provided by Holzapfel [11], and the constitutive models for mitral valves are adopted from May-Newman and Yin [1] and Holzapfel *et al.* [12]. Related stress–strain relationships and their linearizations are provided

and implemented in the user-defined subroutine UMAT within the finite element program ABAQUS. The section on numerical examples documents a single element equibiaxial test simulation, then an analysis in which the applied loads are out of plane, and finally a simulation of mitral valve leaflets is conducted.

2. CONTINUUM MECHANICAL FRAMEWORK AND MATERIAL MODELS

2.1. Kinematics

In the present study, Ω_0 and Ω represent the reference and current configurations, respectively. We consider the deformation map $\boldsymbol{\varphi}(\mathbf{X}) : \Omega_0 \rightarrow \mathbf{R}^3$, which transforms the referential position $\mathbf{X} \in \Omega_0$ of a point into the related current position $\mathbf{x} = \boldsymbol{\varphi}(\mathbf{X}) \in \Omega$. Hence, the deformation gradient \mathbf{F} is defined as $\mathbf{F} = \partial \boldsymbol{\varphi}(\mathbf{X}) / \partial \mathbf{X} = \partial \mathbf{x} / \partial \mathbf{X}$, with the volume ratio $J = \det \mathbf{F} > 0$ ($J = 1$ for an incompressible material). The right and left Cauchy–Green tensors are defined, respectively as $\mathbf{C} = \mathbf{F}^T \mathbf{F}$ and $\mathbf{B} = \mathbf{F} \mathbf{F}^T$.

The model presented in this paper is developed for membraneous or thin shell-like sheets considering that the stress state is plane throughout the sheet. ABAQUS/Standard uses a right-handed local orthonormal system with basis vectors \mathbf{e}_1 and \mathbf{e}_2 located within the sheet and \mathbf{e}_3 normal to it. These basis vectors rotate with the rigid-body motion and the deformations are expressed in this local basis system. Hence, it follows that the deformation gradient may be given in the matrix notation as

$$[\mathbf{F}] = \begin{bmatrix} F_{11} & F_{12} & 0 \\ F_{21} & F_{22} & 0 \\ 0 & 0 & F_{33} \end{bmatrix} \tag{1}$$

Consequently, the components C_{i3} and B_{i3} (for $i \neq 3$) of the related right and left Cauchy–Green matrices are zero. By using the incompressibility condition $J = \det \mathbf{F} = \sqrt{\det \mathbf{C}} = 1$, C_{33} can be expressed in terms of the in plane components, i.e.

$$C_{33} = (C_{11}C_{22} - C_{12}^2)^{-1} \tag{2}$$

2.2. Incompressible transversely isotropic materials

For a material reinforced by one family of fibres, the stress at a material point depends not only on the deformation gradient \mathbf{F} but also on the fibre direction. Hence, we consider a unit vector field $\mathbf{a}_0(\mathbf{X})$ representing the direction of a fibre at point \mathbf{X} in the reference configuration Ω_0 . During deformation the vector \mathbf{a}_0 maps into the related current configuration $\mathbf{a}(\mathbf{X}) = \mathbf{F}(\mathbf{X})\mathbf{a}_0(\mathbf{X})$. Allowing length changes of the fibres, the stretch λ of the fibre along its direction \mathbf{a}_0 is defined as the ratio between the current and the reference configuration, i.e.

$$\lambda^2 = \mathbf{a}_0 \cdot (\mathbf{F}^T \mathbf{F}) \mathbf{a}_0 = \mathbf{a}_0 \cdot \mathbf{C} \mathbf{a}_0 \tag{3}$$

We recall the standard strain-energy function $\tilde{\Psi}$ for transversely isotropic materials, i.e.

$$\tilde{\Psi} = \tilde{\Psi}(\mathbf{C}, \mathbf{a}_0 \otimes \mathbf{a}_0) \tag{4}$$

which is objective since \mathbf{C} and $\mathbf{a}_0 \otimes \mathbf{a}_0$ are material tensor quantities. According to Spencer [13], function (4) may be expressed in terms of five invariants. Thus,

$$\tilde{\Psi}(\mathbf{C}, \mathbf{a}_0 \otimes \mathbf{a}_0) = \Psi^*(I_1, \dots, I_5) \quad (5)$$

where I_1, I_2, I_3 are the three invariants related to isotropic elasticity, while

$$I_4 = \mathbf{a}_0 \cdot \mathbf{C} \mathbf{a}_0, \quad I_5 = \mathbf{a}_0 \cdot \mathbf{C}^2 \mathbf{a}_0 \quad (6)$$

are two pseudo-invariants of \mathbf{C} and $\mathbf{a}_0 \otimes \mathbf{a}_0$. In comparison with (3) we note that I_4 in (6)₁ is the square of the stretch λ in the fibre direction. For incompressible transversely isotropic materials the energy function (5) is modified according to

$$\tilde{\Psi} = \Psi(I_1, I_2, I_4, I_5) + p(J - 1) \quad (7)$$

where the scalar p serves as an indeterminate Lagrange multiplier.

2.2.1. Stress and elasticity tensors. The related stress and elasticity tensors for incompressible transversely isotropic materials can be derived from (7). Hence, the second Piola–Kirchhoff stress tensor \mathbf{S} is

$$\mathbf{S} = 2 \sum_{\substack{i=1 \\ i \neq 3}}^5 \frac{\partial \Psi}{\partial I_i} \frac{\partial I_i}{\partial \mathbf{C}} + p \mathbf{C}^{-1} \quad (8)$$

and the Cauchy stress tensor $\boldsymbol{\sigma} = \mathbf{F} \mathbf{S} \mathbf{F}^T$ may be provided by the push-forward operation of \mathbf{S} to the current configuration. Since the stress component S_{33} is zero for thin sheets we may determine the scalar p from (8). Thus,

$$p = -2 \sum_{\substack{i=1 \\ i \neq 3}}^5 \frac{\partial \Psi}{\partial I_i} \frac{\partial I_i}{\partial C_{33}} C_{33} \quad (9)$$

where C_{33} is provided through Equation (2).

The material elasticity tensor \mathbb{C} results from (8) according to

$$\mathbb{C} = 4 \sum_{\substack{i,j=1 \\ i,j \neq 3}}^5 \frac{\partial^2 \Psi}{\partial I_i \partial I_j} \frac{\partial I_i}{\partial \mathbf{C}} \otimes \frac{\partial I_j}{\partial \mathbf{C}} + 2 \mathbf{C}^{-1} \otimes \frac{\partial p}{\partial \mathbf{C}} + 2p \frac{\partial \mathbf{C}^{-1}}{\partial \mathbf{C}} \quad (10)$$

Note that for the spatial description the elasticity tensor for incompressible materials ($J = 1$) is defined as the push-forward operation of \mathbb{C} as

$$\mathbb{c} = \boldsymbol{\chi}_* (\mathbb{C}), \quad c_{ijkl} = F_{iI} F_{jJ} F_{kK} F_{lL} C_{IJKL} \quad (11)$$

In [11, Section (8.4)], the expression of the linearization of the internal virtual work is provided in index notation, i.e.

$$D_{\Delta \mathbf{u}} \delta W_{\text{int}}(\mathbf{u}, \delta \mathbf{u}) = \int_{\Omega} \frac{\partial \delta u_i}{\partial x_j} (\delta_{ik} \sigma_{jl} + c_{ijkl}) \frac{\partial \Delta u_k}{\partial x_l} dv \quad (12)$$

where the terms $\delta_{ik}\sigma_{jl} + c_{ijkl}$ represent the components of the effective elasticity tensor in the spatial description, and $\delta_{ik}\sigma_{jl}$ is the initial stress contribution. The components c_{ijkl} of \mathbb{c} represent the material contribution to the linearization and are related according to

$$\mathcal{L}_v \boldsymbol{\tau} = \dot{\boldsymbol{\tau}} - \mathbf{l}\boldsymbol{\tau} - \boldsymbol{\tau}\mathbf{l}^T = \mathbb{c} : \mathbf{d} \tag{13}$$

where $\mathcal{L}_v \boldsymbol{\tau}$ is the Lie derivative of the Kirchhoff stress tensor $\boldsymbol{\tau}$ (Oldroyd stress rate), \mathbf{l} is the spatial velocity gradient and \mathbf{d} the (symmetric) rate of deformation tensor.

2.3. Strain-energy functions for mitral valves

2.3.1. Specification of Ψ and issue of polyconvexity. In this work we employ two strain-energy functions with the goal to capture the mechanical response of mitral valve tissue. For example, May-Newman and Yin [1] proposed a transversely isotropic constitutive model, which was developed by a comparison of experimental data obtained from biaxial tensile tests of porcine mitral valve tissue with the constitutive model. Experimental data indicate a highly non-linear mechanical response, and the model in [1] was proposed in terms of the invariants I_1 and I_4 . Thus,

$$\Psi(I_1, I_4) = \bar{c}_0 [\exp^{\bar{c}_1(I_1-3)^2 + \bar{c}_2(\sqrt{I_4}-1)^4} - 1] \tag{14}$$

where $\bar{c}_i, i = 0, 1, 2$, are material parameters.

An alternative function, similar to that proposed by Holzapfel *et al.* [12], is

$$\Psi(I_1, I_4) = c_0 [\exp^{c_1(I_1-3)^2 + c_2(I_4-1)^2} - 1] \tag{15}$$

where $c_i, i = 0, 1, 2$, are material parameters. Note that the part $\exp[c_2(I_4 - 1)^2 - 1]$ of (15), which is related to the response of collagen fibres, resembles the strain-energy function used to capture the mechanical response of arterial walls, which goes back to the work of Holzapfel *et al.* [14]. Both energy expressions are based on an exponential function which is an appropriate function to use for the characterization of the mechanical response of soft biological tissues.

In order to avoid non-physical behaviour of soft biological tissues, the related strain-energy function must be polyconvex. It can be shown that polyconvexity of a (continuous) strain-energy function implies that the corresponding acoustic tensor is elliptic for all deformations, which means from the physical point of view that only real wave speeds occur; then the material is said to be stable. There exists a vast literature on polyconvexity, a term coined by Ball [15]. For the definition and several important results on polyconvexity, see, for example, Hartmann *et al.* [16], Schröder and Neff [17] and the literature cited therein.

Studying the two strain-energy functions introduced above, we may conclude that both functions are polyconvex in the case of incompressibility, as employed here, and under the condition that $I_4 \geq 1$. In particular, as far as the isotropic term $(I_1 - 3)^2$ is concerned, it can be shown that polyconvexity is fulfilled for the case that the related strain energy is isochoric (see Hartmann *et al.* [16]), otherwise (for the compressible case) $|\mathbf{F}|^2$ must be greater or equal to three, which is a severe condition on the isotropic part of the strain-energy function. As far as the function $\sqrt{I_4}$ in (14) is concerned it is straightforward to show that $\sqrt{I_4} = |\mathbf{F}\mathbf{a}_0|$ is convex in \mathbf{F} , and, therefore, that $\exp(\sqrt{I_4})$ is convex in \mathbf{F} . Hence, $\exp(\sqrt{I_4} - 1)^4$ is also convex if and only if $I_4 \geq 1$. The function $\exp(I_4 - 1)^2$ in (15), with condition $I_4 \geq 1$, is also convex with respect to \mathbf{F} . A detailed proof is provided in the appendix of Balzani *et al.* [18].

2.3.2. *Stress–strain relationship and its linearization.* In this section, we develop the stress–strain relationships for the mitral valve tissue by using the strain-energy functions (14), (15). In addition, the related elasticity tensor is provided.

We assume here that the plane of the fibres in which they are embedded coincides with the plane of the sheet. Hence, we may express the vector \mathbf{a}_0 , representing the fibre direction in the reference configuration, and the vector $\mathbf{a} = \mathbf{F}\mathbf{a}_0$, representing the fibre direction in the current configuration, in the base $(\mathbf{e}_1, \mathbf{e}_2, \mathbf{e}_3)$ in form of the matrices

$$[\mathbf{a}_0] = \begin{bmatrix} \cos \theta \\ \sin \theta \\ 0 \end{bmatrix}, \quad [\mathbf{a}] = \begin{bmatrix} F_{11} \cos \theta + F_{12} \sin \theta \\ F_{21} \cos \theta + F_{22} \sin \theta \\ 0 \end{bmatrix} \tag{16}$$

where θ denotes the angle between \mathbf{e}_1 and the fibre direction. We may now derive the following stress functions ψ_1, ψ_4 and constitutive functions ψ_{11}, ψ_{44} :

$$\psi_1 = \frac{\partial \Psi}{\partial I_1}, \quad \psi_4 = \frac{\partial \Psi}{\partial I_4}, \quad \psi_{11} = \frac{\partial^2 \Psi}{\partial I_1 \partial I_1}, \quad \psi_{14} = \frac{\partial^2 \Psi}{\partial I_1 \partial I_4}, \quad \psi_{44} = \frac{\partial^2 \Psi}{\partial I_4 \partial I_4} \tag{17}$$

with the explicit expressions

$$\begin{aligned} \psi_1 &= 2 \bar{c}_0 \bar{c}_1 (I_1 - 3) \exp^{\bar{c}_1(I_1-3)^2 + \bar{c}_2(\sqrt{I_4}-1)^4}, \\ \psi_4 &= \frac{2 \bar{c}_0 \bar{c}_2 (\sqrt{I_4} - 1)^3}{\sqrt{I_4}} \exp^{\bar{c}_1(I_1-3)^2 + \bar{c}_2(\sqrt{I_4}-1)^4} \end{aligned} \tag{18}$$

$$\psi_{11} = [2 \bar{c}_0 \bar{c}_1 + 4 \bar{c}_0 \bar{c}_1^2 (I_1 - 3)^2] \exp^{\bar{c}_1(I_1-3)^2 + \bar{c}_2(\sqrt{I_4}-1)^4} \tag{19}$$

$$\psi_{14} = \frac{4 \bar{c}_0 \bar{c}_1 \bar{c}_2 (I_1 - 3) (\sqrt{I_4} - 1)^3}{\sqrt{I_4}} \exp^{\bar{c}_1(I_1-3)^2 + \bar{c}_2(\sqrt{I_4}-1)^4} \tag{20}$$

$$\begin{aligned} \psi_{44} &= \left[\frac{3 \bar{c}_0 \bar{c}_2 (\sqrt{I_4} - 1)^2 + 4 \bar{c}_0 \bar{c}_2^2 (\sqrt{I_4} - 1)^6}{I_4} - \frac{\bar{c}_0 \bar{c}_2 (\sqrt{I_4} - 1)^3}{I_4^{3/2}} \right] \\ &\quad \times \exp^{\bar{c}_1(I_1-3)^2 + \bar{c}_2(\sqrt{I_4}-1)^4} \end{aligned} \tag{21}$$

for function (14), and

$$\psi_1 = 2 c_0 c_1 (I_1 - 3) \exp^{c_1(I_1-3)^2 + c_2(I_4-1)^2}, \quad \psi_4 = 2 c_0 c_2 (I_4 - 1) \exp^{c_1(I_1-3)^2 + c_2(I_4-1)^2} \tag{22}$$

$$\psi_{11} = 2 c_0 c_1 \exp^{c_1(I_1-3)^2 + c_2(I_4-1)^2} + 4 c_0 c_1^2 (I_1 - 3)^2 \exp^{c_1(I_1-3)^2 + c_2(I_4-1)^2} \tag{23}$$

$$\psi_{14} = 4 c_0 c_1 (I_1 - 3) c_2 (I_4 - 1) \exp^{c_1(I_1-3)^2 + c_2(I_4-1)^2} \tag{24}$$

$$\psi_{44} = 2 c_0 c_2 [1 + 2 c_2 (I_4 - 1)^2] \exp^{c_1(I_1-3)^2 + c_2(I_4-1)^2} \tag{25}$$

for function (15). Hence, the stress tensors, the Lagrange multiplier and the elasticity tensors are determined from the strain-energy function (15). As can be seen from (18)–(21) and (22)–(25), the strain energy (14) leads to a more complex set of equations for the stresses and the tangent stiffness as the strain energy (15) does.

Stress tensors and Lagrange multiplier: The second Piola–Kirchhoff stress tensor \mathbf{S} and the related Cauchy stress tensor $\boldsymbol{\sigma}$ may be derived from (8) (note that the invariants I_2 and I_5 are not present in the employed models (14) and (15)). Thus,

$$\mathbf{S} = 2\psi_1 \mathbf{1} + 2\psi_4 \mathbf{a}_0 \otimes \mathbf{a}_0 + p \mathbf{C}^{-1}, \quad \boldsymbol{\sigma} = 2\psi_1 \mathbf{B} + 2\psi_4 \mathbf{a} \otimes \mathbf{a} + p \mathbf{1} \tag{26}$$

In order to compute the Lagrange multiplier p we recall that for plane stress states, with which we are dealing with, $S_{i3} = 0$ for $i = 1, 2, 3$. Hence, the expression of the Lagrange multiplier is provided through (9), which gives

$$p = -2 \left(\frac{\partial \Psi}{\partial I_1} \frac{\partial I_1}{\partial C_{33}} + \frac{\partial \Psi}{\partial I_4} \frac{\partial I_4}{\partial C_{33}} \right) C_{33} = -2\psi_1 C_{33} \tag{27}$$

where the relations $\partial I_1 / \partial C_{33} = 1$ and $\partial I_4 / \partial C_{33} = 0$ (the third component of $[\mathbf{a}_0]$ in (16)₁ is zero), and abbreviation (17)₁ have been used. It is easy to check that $S_{33} = 0$ by inserting (27)₂ into (26)₁, which shows that the plane stress condition is fulfilled.

Elasticity tensors: The material elasticity tensor is now specified by means of (10), which gives

$$\begin{aligned} \mathbb{C} = & 4\psi_{11} \mathbf{1} \otimes \mathbf{1} + 4\psi_{14} (\mathbf{1} \otimes \mathbf{a}_0 \otimes \mathbf{a}_0 + \mathbf{a}_0 \otimes \mathbf{a}_0 \otimes \mathbf{1}) + 4\psi_{44} \mathbf{a}_0 \otimes \mathbf{a}_0 \otimes \mathbf{a}_0 \otimes \mathbf{a}_0 \\ & + 2\mathbf{C}^{-1} \otimes \frac{\partial p}{\partial \mathbf{C}} + 2p \frac{\partial \mathbf{C}^{-1}}{\partial \mathbf{C}} \end{aligned} \tag{28}$$

where the derivatives $\partial I_1 / \partial \mathbf{C} = \mathbf{1}$ and $\partial I_4 / \partial \mathbf{C} = \mathbf{a}_0 \otimes \mathbf{a}_0$ have been used. The explicit components for the tensor $\partial p / \partial \mathbf{C}$ for the strain-energy function (15) are provided in Appendix A, while the components for the tensor $\partial \mathbf{C}^{-1} / \partial \mathbf{C}$ are given as

$$\left(\frac{\partial \mathbf{C}^{-1}}{\partial \mathbf{C}} \right)_{IJKL} = -\frac{1}{2} (C_{IK}^{-1} C_{JL}^{-1} + C_{IL}^{-1} C_{JK}^{-1}) \tag{29}$$

According to (11) the spatial elasticity tensor is according to

$$\begin{aligned} \mathbb{c} = & 4\psi_{11} \mathbf{B} \otimes \mathbf{B} + 4\psi_{14} (\mathbf{B} \otimes \mathbf{a} \otimes \mathbf{a} + \mathbf{a} \otimes \mathbf{a} \otimes \mathbf{B}) + 4\psi_{44} \mathbf{a} \otimes \mathbf{a} \otimes \mathbf{a} \otimes \mathbf{a} \\ & + 2\mathbf{1} \otimes \left(\mathbf{F} \frac{\partial p}{\partial \mathbf{C}} \mathbf{F}^T \right) - 2p \mathbb{1} \end{aligned} \tag{30}$$

where the push-forward operation of the tensor $-\partial \mathbf{C}^{-1} / \partial \mathbf{C}$ is equal to the fourth-order identity tensor $\mathbb{1}$, i.e.

$$F_{iI} F_{jJ} F_{kK} F_{lL} \left(\frac{\partial \mathbf{C}^{-1}}{\partial \mathbf{C}} \right)_{IJKL} = -\frac{1}{2} (\delta_{ik} \delta_{jl} + \delta_{il} \delta_{jk}) = -(\mathbb{1})_{ijkl} \tag{31}$$

For later use we provide relation (30) also in index notation, which is

$$c_{ijkl} = 4\psi_{11} B_{ij} B_{kl} + 4\psi_{14} (B_{ij} a_k a_l + a_i a_j B_{kl}) + 4\psi_{44} a_i a_j a_k a_l \\ + 2\delta_{ij} F_{kK} F_{lL} \frac{\partial p}{\partial C_{KL}} - p(\delta_{ik} \delta_{jl} + \delta_{il} \delta_{jk}) \quad (32)$$

2.3.3. Implementation of the mitral valve models into ABAQUS. We have implemented the material models (14) and (15) into ABAQUS/standard by using the user-defined subroutine UMAT. Basically, it is required to compute the Cauchy stress components and the tangent stiffness matrix. Although the implementation of the stress components is straightforward it is, however, not so obvious how the tangent stiffness matrix has to be implemented. As it turns out, for shell and membrane elements ABAQUS/Standard uses the Green–Naghdi stress rate, here denoted as $\overset{\nabla}{\boldsymbol{\tau}}$. Hence, this section has the goal to explicitly write down the matrices, which are required for the UMAT subroutine within ABAQUS/standard.

Cauchy stresses: For thin sheets only the three stress components in the plane of the sheet need to be provided. By recalling (26)₂ and (17) the stress matrix becomes

$$[\boldsymbol{\sigma}] = \begin{bmatrix} \sigma_{11} & \sigma_{12} \\ \sigma_{12} & \sigma_{22} \end{bmatrix} \quad (33)$$

with the stress components

$$\sigma_{11} = 2\psi_1 B_{11} + 2\psi_4 a_1 a_1 + p, \quad \sigma_{22} = 2\psi_1 B_{22} + 2\psi_4 a_2 a_2 + p \\ \sigma_{12} = 2\psi_1 B_{12} + 2\psi_4 a_1 a_2 \quad (34)$$

and with the scalar p according to (27).

Tangent modulus related to the Green–Naghdi stress rate. The Green–Naghdi stress rate $\overset{\nabla}{\boldsymbol{\tau}}$ is defined as (see, for example, Simo and Hughes [19] and Holzapfel [11])

$$\overset{\nabla}{\boldsymbol{\tau}} = \dot{\boldsymbol{\tau}} - \boldsymbol{\Omega} \boldsymbol{\tau} + \boldsymbol{\tau} \boldsymbol{\Omega} = \overset{\nabla}{\mathbb{C}} : \mathbf{d} \quad (35)$$

where the abbreviations $\boldsymbol{\Omega} = \dot{\mathbf{R}} \mathbf{R}^T$ for the skew tensor $\boldsymbol{\Omega} = -\boldsymbol{\Omega}^T$, with \mathbf{R} denoting the rotation tensor, and

$$\overset{\nabla}{(\mathbb{C})}_{ijkl} = (\overset{\circ}{\mathbb{C}})_{ijkl} - \Lambda_{iakl} \tau_{aj} + \tau_{ia} \Lambda_{ajkl}, \quad (\overset{\circ}{\mathbb{C}})_{ijkl} = (\mathbb{C})_{ijkl} + \tau_{ik} \delta_{jl} + \delta_{ik} \tau_{jl} \quad (36)$$

have been introduced. Herein the tensor $\overset{\circ}{\mathbb{C}}$ is related to the Jaumann stress rate, \mathbb{C} is the spatial elasticity tensor as provided in Equations (11) and (13), or in the specific form (32), and Λ_{ijkl} are the components of a material-independent fourth-order tensor. A detailed derivative of (36) can be found in Appendix B. Note that it is the expression $\overset{\nabla}{\mathbb{C}} / J$ which is required for the ABAQUS user-defined subroutine UMAT. The stresses in the above relations are already given, what is left are the components $(\mathbb{C})_{ijkl}$, which are provided in the next step.

The general matrix form of the spatial elasticity tensor \mathbb{c} for the specific considered plane stress case reads

$$C_{ijkl} = \begin{bmatrix} C_{1111} & C_{1122} & C_{1112} \\ C_{2211} & C_{2222} & C_{2212} \\ C_{1211} & C_{1222} & C_{1212} \end{bmatrix} \quad (37)$$

For simplicity we adopt the following notation:

$$[\mathbf{D}] = \begin{bmatrix} D_{11} & D_{12} & D_{13} \\ D_{12} & D_{22} & D_{23} \\ D_{13} & D_{23} & D_{33} \end{bmatrix} \quad (38)$$

where symmetry properties have been used. It is now straightforward to derive the components of $[\mathbf{D}]$. From Equation (32) we find that

$$D_{11} = 4(\psi_{11}B_{11}^2 + 2\psi_{14}B_{11}a_1^2 + \psi_{44}a_1^4) + 2F_{1I}F_{1J} \frac{\partial p}{\partial C_{IJ}} - 2p \quad (39)$$

$$D_{12} = 4[\psi_{11}B_{11}B_{22} + \psi_{14}(B_{11}a_2^2 + B_{22}a_1^2) + \psi_{44}a_1^2a_2^2] + (F_{1I}F_{1J} + F_{2I}F_{2J}) \frac{\partial p}{\partial C_{IJ}} \quad (40)$$

$$D_{13} = 4[\psi_{11}B_{11}B_{12} + \psi_{14}(B_{11}a_1a_2 + B_{12}a_1^2) + \psi_{44}a_1^3a_2 + F_{1I}F_{2J}] \frac{\partial p}{\partial C_{IJ}} \quad (41)$$

$$D_{22} = 4(\psi_{11}B_{22}^2 + 2\psi_{14}B_{22}a_2^2 + \psi_{44}a_2^4) + 2F_{2I}F_{2J} \frac{\partial p}{\partial C_{IJ}} - 2p \quad (42)$$

$$D_{23} = 4[\psi_{11}B_{12}B_{22} + \psi_{14}(B_{22}a_1a_2 + B_{12}a_2^2) + \psi_{44}a_1a_2^3 + F_{1I}F_{2J}] \frac{\partial p}{\partial C_{IJ}} \quad (43)$$

$$D_{33} = 4(\psi_{11}B_{12}^2 + 2\psi_{14}B_{12}a_1a_2 + \psi_{44}a_1^2a_2^2) - p \quad (44)$$

where $I, J = 1, 2$. Herein p is obtained by means of Equation (27)₂, $\partial p / \partial C_{IJ}$ is provided in Appendix A, and the constitutive functions are according to (19)–(21) or (23)–(25).

2.3.4. Identification of the material parameters. May-Newman and Yin [1] used three experimental protocols (off-biaxial, strip biaxial circumferential, strip biaxial radial) to determine the average material parameters \bar{c}_0 , \bar{c}_1 and \bar{c}_2 of the strain-energy function (14) for anterior and posterior leaflets. A set of average material parameters are provided in Table I. The values in Table I indicate that \bar{c}_0 and \bar{c}_1 are similar for both leaflets, while \bar{c}_2 is much greater in the anterior leaflets.

We identified now the material parameters c_0 , c_1 and c_2 of the strain-energy function (15) by fitting the related stress–stretch relations to the stress–stretch relations of the model (14), as proposed by May-Newman and Yin [1], using four sets of biaxial tests (equibiaxial, off-biaxial, strip

Table I. Average material parameter values for the strain-energy function by May-Newman and Yin [1] according to Equation (14).

	\bar{c}_0 (kPa)	\bar{c}_1	\bar{c}_2
Anterior leaflet	0.399	4.325	1446.5
Posterior leaflet	0.414	4.848	305.4

Note: Values are adopted from [1, Table 4].

Table II. Average material parameter values for the strain-energy function (15).

	c_0 (kPa)	c_1	c_2
Anterior leaflet	0.0520	4.63	22.6
Posterior leaflet	0.171	5.28	6.46

biaxial fixed in fibre direction, strip biaxial fixed perpendicular to fibre direction). In these tests for the anterior and posterior leaflets, the fibre direction was aligned with one of the principal stretch directions. For each leaflet (anterior and posterior) we identified one set of material parameters. For the fitting process we used the function *lsqnonlin* in the Optimization Toolbox of Matlab together with the Levenberg–Marquardt algorithm. The identified average material parameters of the strain-energy function (15) are summarized in Table II.

The related plots are provided in the Figures 1 and 2, show satisfying agreement.

3. NUMERICAL EXAMPLES

3.1. Equibiaxial test simulation

Displacement-controlled single element tests were carried out in order to check the proper implementation of the stress and tangent stiffness updates within ABAQUS. For this equibiaxial test simulation, a four-noded membrane element (ABAQUS element type M3D4) was used. The fibre direction and its perpendicular were aligned with the principal stretch directions, and material parameters taken from Table II.

The nodal displacements of the element were imposed as boundary conditions, principal stretches were determined, and related theoretical Cauchy stresses were calculated from (34). The theoretical Cauchy stresses were then compared with those obtained from the finite element analysis, see Figure 3.

As can be seen, the single element equibiaxial test illustrates an excellent agreement between the theoretical and the numerical solutions.

3.2. Out-of-plane loading

The objective of this section is the test of the mitral valve material model behaviour in the case of out-of-plane loading. Considering the literature, much information on numerical simulation of

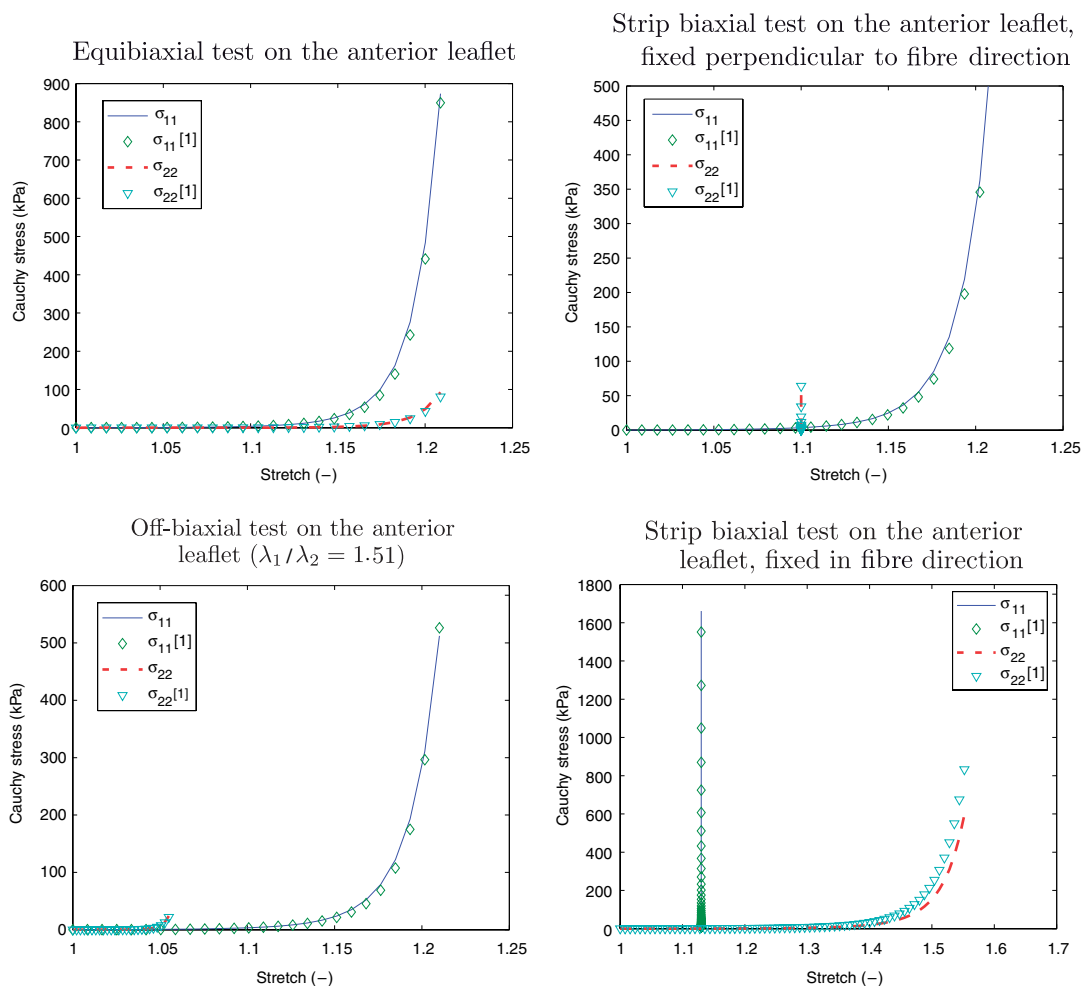


Figure 1. Cauchy stress–stretch curves for the anterior leaflets: comparison between the constitutive model by May-Newman and Yin [1], i.e. Equation (14), with material parameters from Table I, and the constitutive model (15), with material parameters from Table II. Stress values σ_{11} are in the fibre direction, and σ_{22} perpendicular to it.

planar systems is available; however, cases of transversely isotropic hyperelastic models combined with out-of-plane loading, such as the case for mitral valve leaflets subject to ventricle pressure, are scarce.

In [20] a phenomenological model for an incompressible transversely isotropic material was proposed. It is important to note that the model uses eight material parameters, and is therefore of limited use. We focus on an example described therein. It is a spherical balloon, made of this transversely isotropic material, and subjected to an internal pressure. For the purpose of comparison we have now fitted the mitral valve material to the model in [20], and have used the same non-linear least-square technique, as described in Section 2.3.4, in order to obtain the material parameters of

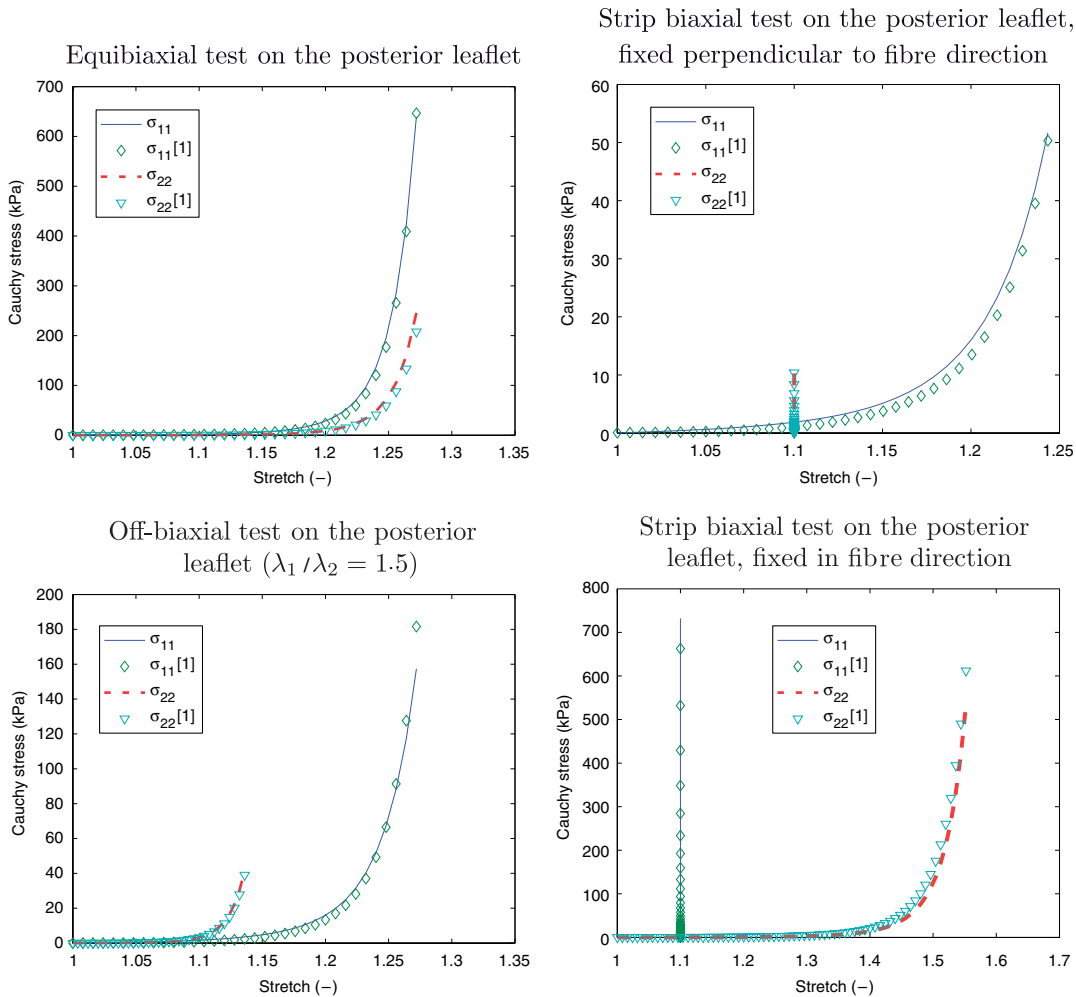


Figure 2. Cauchy stress–stretch curves for the posterior leaflets: comparison between the constitutive model by May-Newman and Yin [1], i.e. Equation (14), with material parameters from Table I, and the constitutive model (15), with material parameters from Table II. Stress values σ_{11} are in the fibre direction, and σ_{22} perpendicular to it.

the strain-energy function (15). The mitral valve constitutive model was fit to an equibiaxial test and an off-biaxial test. The following parameters for the mitral valve strain-energy function were obtained: $c_0 = 86.1$, $c_1 = 0.0059$ and $c_2 = 0.031$. Note that all the material parameters provided in [20] were without units.

Next, a spherical balloon made of the mitral valve material was subjected to an internal pressure. The collagen fibres were arranged in the circumferential direction such that the problem is axisymmetric.

The analysis was performed on one-eighth of the structure, see Figure 4. The balloon has a radius of 10 and a thickness of 0.5. It was meshed with three-noded shell elements (ABAQUS

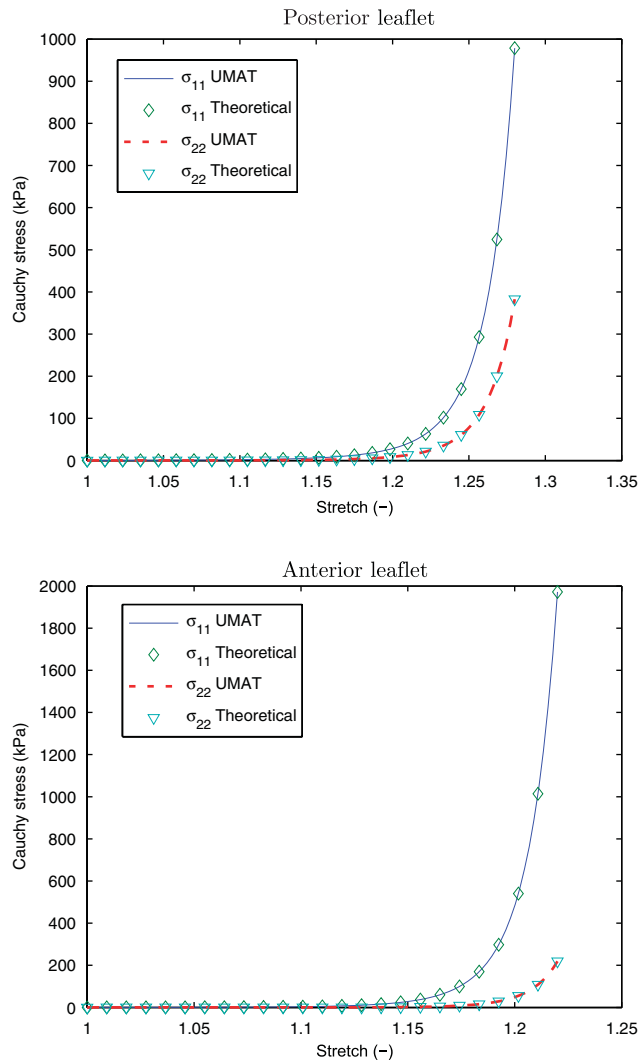


Figure 3. Cauchy stress–stretch curves for a single element equibiaxial test for the anterior and posterior leaflets: comparison of theoretical Cauchy stresses with numerical stresses obtained from the UMAT subroutine. Stress values σ_{11} are in the fibre direction, and σ_{22} perpendicular to it.

type S3). After inflation the initially spherical balloon took on the shape of a rugby ball, see Figure 5. In Figure 6 the pressure–displacement relationships of two radial points A and B (see Figure 4) are plotted and compared with the results documented in [20].

The differences observed in Figure 6 can be explained by the fact that the two strain-energy functions have very different forms. The function in [20] is based on Ogden’s material model, includes 8 material parameters, and is more adapted for rubber-like materials, which can undergo stretches up to 10. Our function (15) is based on an exponential form, includes 3 material parameters, and is more adapted for soft biological tissues, which undergo stretches in the order of 1.5.

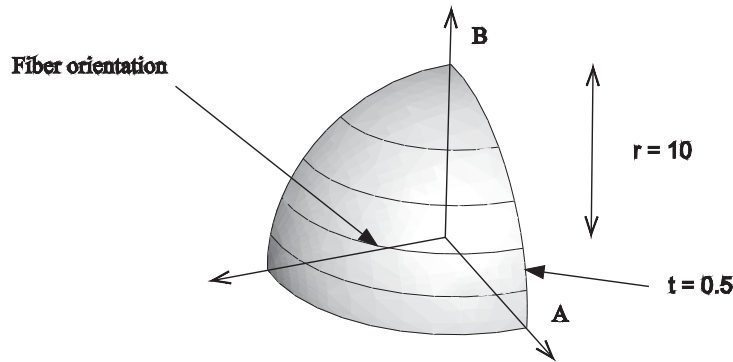


Figure 4. Geometry of a balloon made of transversely isotropic material. Only one-eighth of the structure is shown.

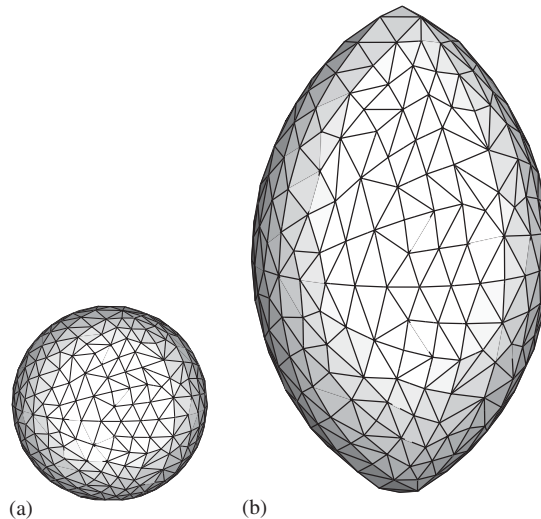


Figure 5. Inflation of a spherical balloon made of transversely isotropic material: (a) initial and (b) current configuration.

Anyway, these results appear to be close enough in order to conclude that the stress and tangent stiffness updates for the mitral valve model are properly implemented for out-of-plane loading.

Finally, this inflation test was carried out with the material model related to Equation (14), as proposed by May-Newman and Yin [1], with the material parameters in Table I for the anterior leaflet, and for the material model related to Equation (15), with the material parameters in Table II for the anterior leaflet. In Figure 7 the pressure–displacement relationships of the two radial points A and B (see Figure 4) are plotted for both material models. As can be seen, quite a difference appears in the global pressure–displacement response.

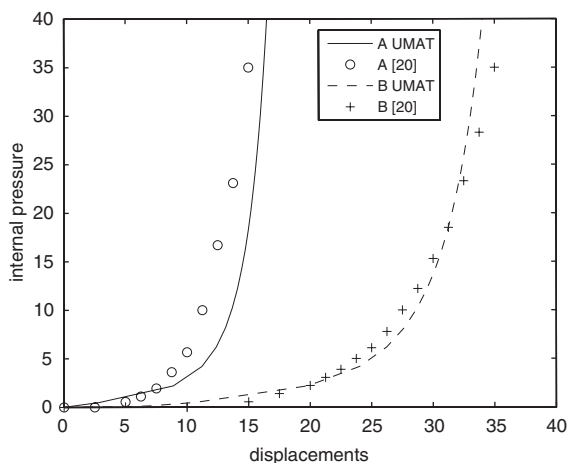


Figure 6. Inflation of a spherical balloon made of a transversely isotropic material: pressure–displacement relationships of two radial points A and B (see Figure 4).

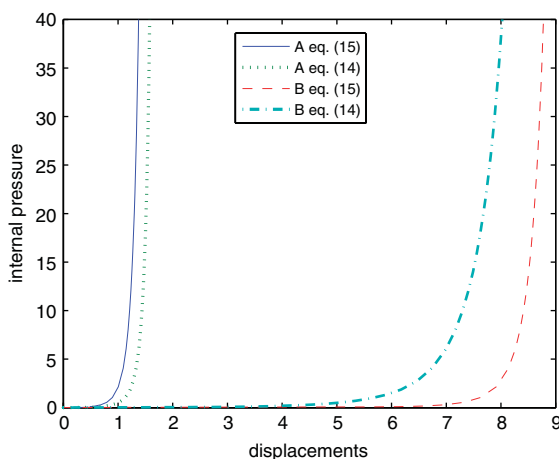


Figure 7. Inflation of a spherical balloon made of a material to be described by (14) and (15): pressure–displacement relationships of two radial points A and B (see Figure 4).

3.3. Initial simulations of mitral valve leaflets

In this section, we present a three-dimensional finite element model of the porcine mitral valve that simulates a part of the heart cycle: starting at the end of diastole and ending at the maximum pressure in the left ventricle (i.e. about the middle of the ejection phase). In the healthy mitral valve, two types of chordae tendinae are present; these are the marginal chordae attached to the free edge of the leaflets and the strut chordae attached beyond the free edge and the average total number of chordae is 25, see Lam *et al.* [21]. Elongation or rupture of the chordae (pathological state) can lead to mitral valve prolapse, which allows the leaflets to buckle back into the left atrium

during the heart's contraction. This may lead to backward leaking of blood into the left atrium. In this study, two simulations were performed with different types of chordae tendinae: the first one with marginal chordae only (pathological state) and the second one with marginal and strut chordae (healthy state).

3.3.1. Geometry, material and boundary conditions. After the three-dimensional ultrasound measurements were carried out on the heart of the anaesthetized animal, the dimensions of the porcine mitral valve were measured post mortem. The diameter of the annulus was 22 mm, and the annulus was assumed to be flat. The length of the anterior and posterior leaflets were measured to be 16 and 8 mm, respectively. The thickness of the leaflet was assumed to be constant and equal to 1 mm. In order to simplify the model, the commissures of the mitral valve were not represented in the model. Twenty chordae tendinae were attached to the edge of the leaflets, while the cross section area of each chordae was assumed to be 1 mm².

The constitutive model (15) was used for both leaflets taking the material parameters from Table II. For the chordae, an isotropic incompressible hyperelastic material model was implemented into the ABAQUS/Standard subroutine UHYPER. The material model was derived from the following strain-energy function U :

$$U(I_1) = a_1(I_1 - 3) + a_2[\exp^{a_3(I_1 - 3)} - 1] \quad (45)$$

where a_1 , a_2 and a_3 are the material parameters. In order to determine a realistic material model the stress–strain behaviour of the chordae tendinae in uniaxial tension, as published by Kunzelman and Cochran [22], was used. The direction of the leaflet collagen fibres was assumed to be oriented concentric to the mitral annulus [1].

The leaflets were meshed with triangular membrane elements M3D3 and the chordae tendinae with truss elements T3D2. The nodes along the annulus were free to rotate in every direction but their translations were constrained, i.e. the annulus was acting as an axis of rotation for the leaflets. The translations were constrained at the attachment between the chordae and the papillary muscles. We assumed fixed boundary conditions for the papillary muscles (see Figure 8).

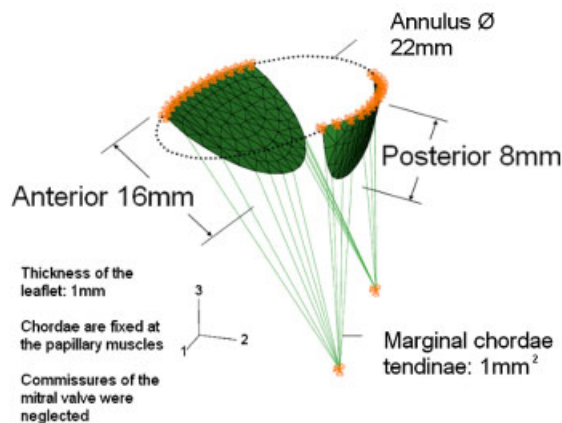


Figure 8. Initial geometry of the valve at the beginning of systole with related boundary conditions.

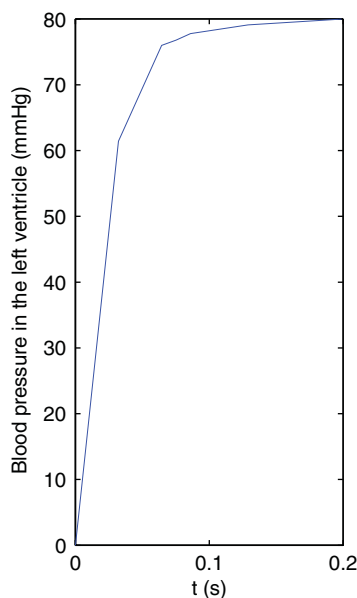


Figure 9. Measured blood pressure in the left ventricle of the pig during the isovolumetric contraction phase up to the maximum pressure in the left ventricle in the ejection phase applied as load history on the leaflets.

In order to prevent the leaflets from interpenetrating each other upon closure, a contact condition was set between the two surfaces. The measured blood pressure in the left ventricle of the pig during the isovolumetric contraction phase up to the maximum pressure in the left ventricle in the ejection phase was applied as load history, see Figure 9.

3.3.2. Results. The first simulation considered only marginal chordae, i.e. related to a pathological state. After about 70% of the peak pressure the leaflets did not move much, i.e. the main motion occurred up to this point in time. Figure 10 shows the position at the end of the simulation at maximum ventricle pressure. In Figure 11 the pressure–displacement relationships of a node located in the middle of the anterior leaflet are plotted. The quality of the ultrasound measurements carried out on the pig was too poor; hence, the finite element results of the displacement in the 3-direction are compared with those obtained from the ultrasound measurements carried out on a healthy 25-year-old human male. The numerical values of the displacement in the 3-direction in the higher pressure domain are larger than the displacement taken from the ultrasound measurement. The displacement of the same node in the 2-direction, i.e. towards the posterior leaflet, shows that the area of coaptation (i.e. area in contact) between the two leaflets reaches its maximum and remains constant after a pressure of 30 mmHg.

Next, in order to reduce the displacement of the anterior leaflet in the 3-direction, strut chordae (i.e. chordae attached beyond the free edge of the leaflet) were attached to the anterior leaflet in addition to the marginal chordae already attached. Hence, an FE analysis with six strut chordae,

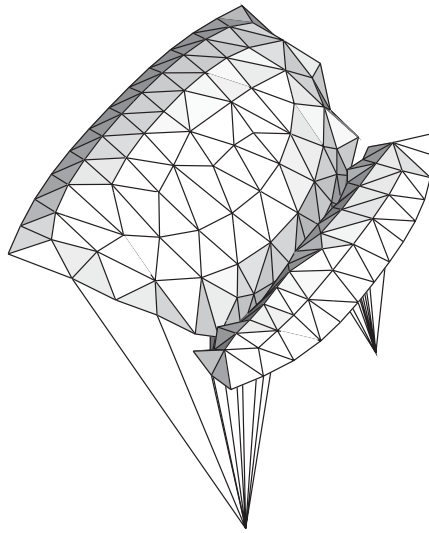


Figure 10. Position of the mitral valve at the end of the simulation at maximum ventricle pressure, utilizing marginal chordae only.

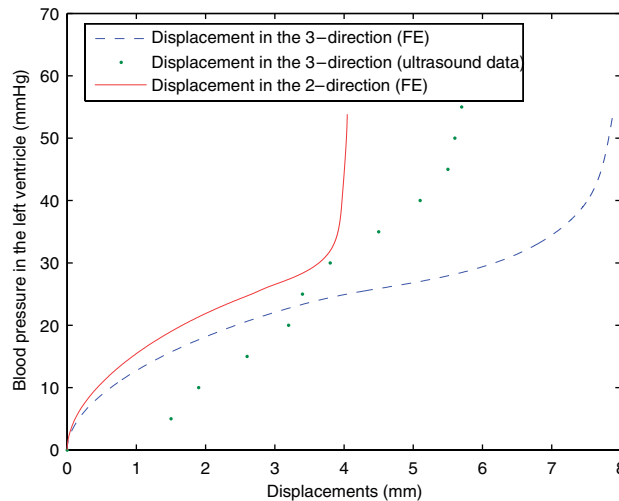


Figure 11. Left ventricle blood pressure *versus* the computed displacements in the 2-direction (towards the posterior leaflet) and the 3-direction for a node located at the middle of the anterior leaflet. The model considers marginal chordae, i.e. related to a pathological state. The dots show the measured data of the corresponding node obtained from the ultrasound measurements carried out on the human valve. For the related directions see Figure 8.

i.e. related to a healthy state, was performed. In Figure 12 the blood pressure in the left ventricle is plotted *versus* the displacements in the 3-direction. It is worth noting that the accuracy of the first four measurement points is not certain; however, the remaining points have high accuracy. As

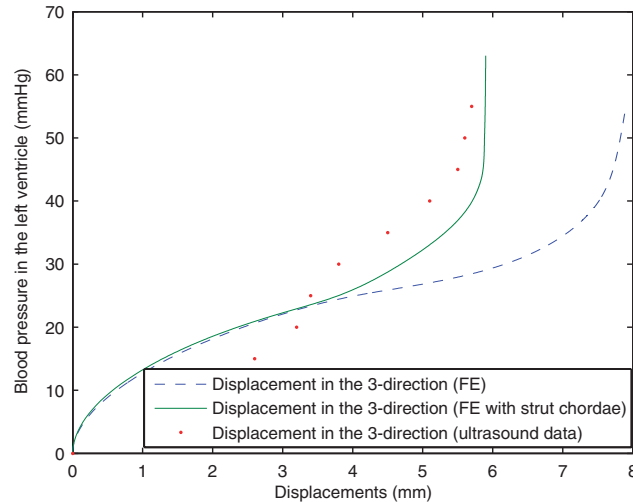


Figure 12. Left ventricle blood pressure *versus* the computed displacements in the 3-direction for a node located in the middle of the anterior leaflet. The model represents a healthy state. The dashed curve shows the pressure–displacement relationship for the model with marginal chordae (pathological state), see also Figure 11, while the solid curve shows the pressure–displacement relationship for the model with marginal and strut chordae (healthy state). The dots show the measured data of the corresponding node obtained from the ultrasound measurements carried out on the human valve. For the related directions see Figure 8.

can be seen from Figure 12 the simulation is in relatively good agreement with the experimental data.

Additional analyses of the mitral apparatus using the present material model for the leaflets are presented by Prot and Skallerud [23] where the influence of the shape of the annulus (flat *versus* saddle-shaped annulus) on the force distribution in the chordae and on the stress state of the leaflets is investigated. A pathological state without strut chordae attached to the anterior leaflet is also studied in detail.

4. CONCLUDING REMARKS

In this study an efficient implementation of a transversely isotropic hyperelastic material model is presented. Incompressibility is accounted for, and a polyconvex strain-energy function is employed and fitted to mitral valve tissue test results. The material model, which is also used for the simulation of blood vessels, seems to be more robust and provide faster computational results than the alternative, as proposed in [1]. In addition to the polyconvexity fulfilment, the model only requires three material parameters. With the implemented model one has a tool available that allows the simulation of mitral valve response for both healthy and diseased conditions. The model will, however, be further validated against ultrasound measurements of higher resolution in the future. This also opens up for determination of *in vivo* material parameters using inverse methods.

APPENDIX A

Component expressions for $\partial p/\partial \mathbf{C}$: Recall matrix (16)₁ and introduce the abbreviations $a_{01} = \cos \theta$ and $a_{02} = \sin \theta$ so that $[\mathbf{a}_0] = [a_{01} \ a_{02} \ 0]^T$. Now, we provide the explicit expressions for the tensor $\partial p/\partial \mathbf{C}$, which reads in index notation

$$\left(\frac{\partial p}{\partial \mathbf{C}}\right)_{IJ} = \frac{\partial p(C_{11}, C_{22}, C_{12})}{\partial C_{IJ}} \quad (\text{A1})$$

By recalling the derivatives $\partial I_1/\partial \mathbf{C} = \mathbf{1}$ and $\partial I_4/\partial \mathbf{C} = \mathbf{a}_0 \otimes \mathbf{a}_0$ we find the components of (A1) as

$$\begin{aligned} \frac{\partial p}{\partial C_{11}} = & -4c_0c_1\{(1 - C_{22}C_{33}^2) + (I_1 - 3)[2c_1(I_1 - 3)(1 - C_{22}C_{33}^2) + 2c_2(I_4 - 1)a_{01}^2] \\ & - (I_1 - 3)C_{22}C_{33}\}C_{33} \exp^{c_1(I_1-3)^2+c_2(I_4-1)^2} \end{aligned} \quad (\text{A2})$$

$$\begin{aligned} \frac{\partial p}{\partial C_{22}} = & -4c_0c_1\{(1 - C_{22}C_{33}^2) + (I_1 - 3)[2c_1(I_1 - 3)(1 - C_{22}C_{33}^2) + 2c_2(I_4 - 1)a_{02}^2] \\ & - (I_1 - 3)C_{11}C_{33}\}C_{33} \exp^{c_1(I_1-3)^2+c_2(I_4-1)^2} \end{aligned} \quad (\text{A3})$$

$$\begin{aligned} \frac{\partial p}{\partial C_{12}} = & -4c_0c_1\{2C_{12}C_{33}^2 + (I_1 - 3)[4c_1(I_1 - 3)C_{12}C_{33}^2 + 4c_2(I_4 - 1)a_{01}a_{02}] \\ & + 2(I_1 - 3)C_{12}C_{33}\}C_{33} \exp^{c_1(I_1-3)^2+c_2(I_4-1)^2} \end{aligned} \quad (\text{A4})$$

APPENDIX B

Derivative of Equation (36): Before deriving Equation (36) we recall the relation for the Jaumann–Zaremba stress rate $\dot{\boldsymbol{\tau}}$, which is used in ABAQUS/Standard for continuum elements. Starting from (13) and using the split $\mathbf{I} = \mathbf{d} + \mathbf{w}$, where \mathbf{w} is the spin tensor, we deduce that

$$\dot{\boldsymbol{\tau}} - \mathbf{w}\boldsymbol{\tau} + \boldsymbol{\tau}\mathbf{w} = \mathbb{C} : \mathbf{d} + \boldsymbol{\tau}\mathbf{d} + \mathbf{d}\boldsymbol{\tau} \quad (\text{B1})$$

where the left-hand side is $\dot{\boldsymbol{\tau}}$ (see, e.g. [11]). Hence $\dot{\boldsymbol{\tau}} = \mathbb{C} : \mathbf{d} + \boldsymbol{\tau}\mathbf{d} + \mathbf{d}\boldsymbol{\tau}$, and, consequently,

$$\dot{\boldsymbol{\tau}} = \dot{\mathbb{C}} : \mathbf{d}, \quad (\dot{\mathbb{C}})_{ijkl} = (\mathbb{C})_{ijkl} + \tau_{ik}\delta_{jl} + \delta_{ik}\tau_{jl} \quad (\text{B2})$$

where $\dot{\mathbb{C}}$ is the Jaumann–Zaremba tangent moduli and $(\dot{\mathbb{C}})_{ijkl}$ the related components.

Now, by taking (B1) and adding the terms $\boldsymbol{\tau}\boldsymbol{\Omega} - \boldsymbol{\Omega}\boldsymbol{\tau}$ to the left- and right-hand sides, with the skew tensor $\boldsymbol{\Omega} = \mathbf{R}\mathbf{R}^T$, we get

$$\dot{\boldsymbol{\tau}} - \boldsymbol{\Omega}\boldsymbol{\tau} + \boldsymbol{\tau}\boldsymbol{\Omega} = \mathbb{C} : \mathbf{d} + \boldsymbol{\tau}\mathbf{d} + \mathbf{d}\boldsymbol{\tau} + (\mathbf{w} - \boldsymbol{\Omega})\boldsymbol{\tau} - \boldsymbol{\tau}(\mathbf{w} - \boldsymbol{\Omega}) \quad (\text{B3})$$

where the left-hand side is the Green–Naghdi Stress rate $\overset{\nabla}{\boldsymbol{\tau}}$ according to (35)₁, and hence

$$\overset{\nabla}{\boldsymbol{\tau}} = \dot{\boldsymbol{\tau}} + (\mathbf{w} - \boldsymbol{\Omega})\boldsymbol{\tau} - \boldsymbol{\tau}(\mathbf{w} - \boldsymbol{\Omega}) \quad (\text{B4})$$

Mehrabadi and Nemat-Nasser [24] showed that the term $(\mathbf{w} - \mathbf{\Omega})$ can be expressed as

$$\mathbf{w} - \mathbf{\Omega} = \mathbf{\Lambda} : \mathbf{d} \quad (\text{B5})$$

where $\mathbf{\Lambda}$ is a fourth-order tensor defined through Equation (7.3.12b) in Simo and Hughes [19]. By substituting (B5) in (B4) we may obtain in index notation

$$\overset{\nabla}{\tau}_{ij} = [(\overset{\nabla}{\mathbb{C}})_{ijkl} - \Lambda_{iakl}\tau_{aj} + \tau_{ia}\Lambda_{ajkl}]d_{kl} \quad (\text{B6})$$

where the terms between the brackets yield the desired result, i.e. the components of the non-symmetric Green–Naghdi tangent moduli $(\overset{\nabla}{\mathbb{C}})_{ijkl}$ according to (36)₁.

ACKNOWLEDGEMENTS

The authors are grateful to professor J. Schröder for helpful input on the issue of tangent moduli.

REFERENCES

1. May-Newman K, Yin FCP. A constitutive law for mitral valve tissue. *Journal of Biomechanical Engineering* 1998; **120**:38–47.
2. Kunzelman KS, Cochran RP, Chuong C, Ring WS, Verrier ED, Eberhart RD. Finite element analysis of the mitral valve. *Journal of Heart Valve Disease* 1993; **2**:326–340.
3. Einstein DR, Kunzelman K, Reinhall P, Nicosia M, Cochran RP. Haemodynamic determinants of the mitral valve closure sound: a finite element study. *Medical and Biological Engineering and Computing* 2004; **42**:832–846.
4. Votta E, Maisano F, Soncini M, Redaelli A, Montevocchi FM, Alfieri O. 3-D computational analysis of the stress distribution on the leaflets after edge-to-edge repair of mitral regurgitation. *Journal of Heart Valve Disease* 2002; **11**:810–822.
5. Dal Pan F, Donzella G, Fucci C, Schreiber M. Structural effects of an innovative surgical technique to repair heart valve defects. *Journal of Biomechanics* 2005; **38**:2460–2471.
6. Einstein DR, Reinhall P, Nicosia M, Cochran RP, Kunzelman K. Dynamic finite element implementation of nonlinear, anisotropic hyperelastic biological membranes. *Computer Methods in Biomechanics and Biomedical Engineering* 2003; **6**:33–44.
7. Gruttmann F, Taylor RL. Theory and finite element formulation of rubberlike membrane shells using principal stretches. *International Journal for Numerical Methods in Engineering* 1992; **35**:1111–1126.
8. Holzapfel GA, Eberlein R, Wriggers P, Weizsäcker HW. Large strain analysis of soft biological membranes: formulation and finite element analysis. *Computer Methods in Applied Mechanics and Engineering* 1996; **132**: 45–61.
9. Weiss JA, Maker BN, Govindjee S. Finite element implementation of incompressible, transversely isotropic hyperelasticity. *Computer Methods in Applied Mechanics and Engineering* 1996; **135**:107–128.
10. Sun W, Sacks MS. Finite element implementation of a generalized fung-elastic constitutive model for planar soft tissues. *Biomechanics and Modeling in Mechanobiology* 2005; **4**:190–199.
11. Holzapfel GA. *Nonlinear Solid Mechanics. A Continuum Approach for Engineering*. Wiley: Chichester, 2000.
12. Holzapfel GA, Sommer G, Gasser CT, Regitnig P. Determination of the layer-specific mechanical properties of human coronary arteries with non-atherosclerotic intimal thickening, and related constitutive modelling. *American Journal of Physiology-Heart and Circulatory Physiology* 2005; **289**:H2048–H2058.
13. Spencer AJM. Constitutive theory for strongly anisotropic solids. In *Continuum Theory of the Mechanics of Fibre-Reinforced Composites*, Spencer AJM (ed.). CISM Courses and Lectures, vol. 282, International Centre for Mechanical Sciences. Springer: Wien, 1984; 1–32.
14. Holzapfel GA, Gasser TC, Ogden RW. A new constitutive framework for arterial wall mechanics and a comparative study of material models. *Journal of Elasticity* 2000; **61**:1–48.
15. Ball JM. Convexity conditions and existence theorems in nonlinear elasticity. *Archive for Rational Mechanics and Analysis* 1977; **63**:337–403.

16. Hartmann S, Neff P. Polyconvexity of generalized polynomial type hyperelastic strain energy functions for near-incompressibility. *International Journal of Solids and Structures* 2003; **40**:2767–2791.
17. Schröder J, Neff P. Invariant formulation of hyperelastic transverse isotropy based on polyconvex free energy functions. *International Journal of Solids and Structures* 2003; **40**:401–445.
18. Balzani D, Neff P, Schröder J, Holzapfel GA. A polyconvex framework for soft biological tissues. Adjustment to experimental data. *International Journal of Solids and Structures* 2006; **43**:6052–6070.
19. Simo JC, Hughes TJR. *Computational Inelasticity*. Springer: New York, 1998.
20. Itskov M. A generalized orthotropic hyperelastic material model with application to incompressible shells. *International Journal for Numerical Methods in Engineering* 2001; **50**:1777–1799.
21. Lam JH, Ranganathan N, Wigle ED, Silver MD. Morphology of the human mitral valve: I. Chordae tendinae: a new classification. *Circulation* 1970; **41**:449–458.
22. Kunzelman KS, Cochran RP. Mechanical properties of basal and marginal mitral valve chordae tendinae. *ASAIO Transactions* 1990; **36**:M405–M408.
23. Prot V, Skallerud B. Finite element analysis of the mitral apparatus: annulus shape effect and chordal force distribution. 2006, submitted.
24. Mehrabadi MM, Nemat-Nasser S. Some basic kinematical relations for finite deformations of continua. *Mechanics of Materials* 1987; **6**:127–138.